Imaginary-time-enhanced feedback-based quantum algorithms for ground-state preparation

Thanh Nguyen Van Long [1,2] Lan Nguyen Tran [1,2] and Le Bin Ho [3,4,*]

[1] *Faculty of Physics and Engineering Physics, University of Science, Ho Chi Minh City 70000, Vietnam*

[2] *Vietnam National University, Ho Chi Minh City 70000, Vietnam*

[3] *Frontier Research Institute for Interdisciplinary Sciences, Tohoku University, Sendai 980-8578, Japan*

[4] *Department of Applied Physics, Graduate School of Engineering, Tohoku University, Sendai 980-8579, Japan*

(Received 16 December 2025; revised 25 January 2026; accepted 21 October 2026; published 2 November 2026)

Preparing ground states of strongly correlated quantum systems is a central goal in quantum simulation and optimization. The feedback-based quantum algorithm (FALQON) provides an attractive alternative to variational methods with a fully quantum feedback rule, but it fails in the presence of spectral degeneracies, where the feedback signal collapses and the evolution cannot reach the ground state. Using the Fermi-Hubbard model on lattices up to 3×3, we show that this breakdown appears at half filling on the 2×2 lattice and extends to both half-filled and doped configurations on the 3×3 lattice. We then introduce an imaginary-time-enhanced FALQON (*i*FALQON) scheme, which inserts short imaginary-time evolution steps into the feedback loop. This proposed method suppresses excited-state components, escapes degenerate subspaces, restores monotonic energy descent, and improves ground-state convergence across the tested fillings. We further benchmark its performance against existing methods, showing improved results for *i*FALQON, demonstrating the potential of hybrid real-imaginary-time feedback dynamics for ground-state preparation in strongly correlated quantum systems.

DOI: 10.1103/cbcv-fnm2

I. INTRODUCTION

Preparing ground states of strongly correlated quantum systems is a central task in quantum chemistry, condensed-matter physics, and quantum information science [1,2]. Hybrid quantum-classical approaches, e.g., variational quantum eigensolver (VQE) [3] and quantum approximate optimization algorithm (QAOA) [4], have been widely explored for this purpose. However, their performance is tied to high-dimensional classical parameter optimization and problem-specific ansätze, which become increasingly fragile under barren plateaus, noise accumulation, and expressibility constraints [5,6]. These limitations motivate a different paradigm, i.e., feedback-driven quantum optimization schemes in which all control parameters are generated intrinsically by the quantum dynamics.

The feedback-based algorithm for quantum optimization (FALQON) [7] exemplifies this paradigm. Instead of minimizing a classical loss landscape, FALQON directly embeds a Lyapunov-style feedback [8] into the Hamiltonian evolution, $H(t) = H_p + \beta(t)H_d$, where the control field $\beta(t)$ is determined from the commutator signal $A(t) = i\langle[H_d, H_p]\rangle_t$ to enforce a monotonic decrease of the cost function $C(t) = \langle H_p\rangle_t$ [8,9]. Recent applications demonstrate that FALQON can efficiently prepare ground states of spin systems, molecular Hamiltonians, and fermionic lattice models in nondegenerate regimes [7,10–12].

Compared with variational approaches such as VQE [3], ADAPT-VQE [13], or QAOA [4], FALQON requires no classical parameter optimization and no problem-specific ansätze design, which avoids well-known challenges including barren plateaus, optimizer instability, and limited expressibility [6]. Existing studies have largely addressed nondegenerate Hamiltonians, and the behavior of feedback-driven optimization in spectrally degenerate regimes remains unexplored.

In this work, we identify a structural failure of FALQON when applied to systems with degenerate spectra, using the Fermi-Hubbard (FH) model as a controlled test bed [14]. Across multiple lattice sizes up to 3×3, we find that FALQON converges reliably in doped configurations but consistently stalls at half filling, where particle-hole symmetry generates degenerate manifolds of low-lying states. When the energy trajectory encounters such a manifold, the commutator signal $A(t)$ becomes strongly suppressed, resulting in feedback amplitudes $\beta(t)$ that oscillate weakly around zero. These nearly vanishing controls are insufficient to induce further transitions and the energy $E(t) = \langle H_p\rangle_t$ becomes trapped above the true ground state.

To resolve this obstruction, we introduce an imaginary-time-enhanced variant [15,16], *i*FALQON, in which short imaginary-time evolution (ITE) steps generated by H_p are periodically inserted into the feedback loop. Imaginary-time propagation effectively damps excited-state components [15–21] while preserving the Lyapunov-based descent structure, allowing the dynamics to escape degenerate subspaces and continue toward the ground state. We provide a convergence analysis for the scheme and benchmark its performance on FH lattices up to 3×3, showing monotonic energy descent

*Contact author: ho.bin.le.e3@tohoku.ac.jp

Published by the American Physical Society under the terms of the Creative Commons Attribution 4.0 International license. Further distribution of this work must maintain attribution to the author(s) and the published article's title, journal citation, and DOI.

and high-fidelity ground-state preparation across all fillings within shallow simulation time step. These results demonstrate that *i*FALQON provides an effective proof-of-concept framework for improving ground-state convergence in correlated many-body systems.

The structure of the paper is as follows: Section II presents the FALQON framework and discusses its limitations. In Sec. III, we introduce the *i*FALQON framework. Its application to the FH model is demonstrated in Sec. IV. In Sec. V, we compare our approach with other existing frameworks. Section VI concludes the paper.

II. FALQON FRAMEWORK

Consider a time-dependent Hamiltonian

$$H(t) = H_p + \beta(t)H_d, \tag{1}$$

where H_p is a problem Hamiltonian whose ground state we seek to prepare, H_d is a driver Hamiltonian, and $\beta(t)$ is a feedback control updated recursively from the system state, which is constructed to enforce a monotonic decrease in a cost function $C(t) = \langle\psi(t)|H_p|\psi(t)\rangle = \langle H_p\rangle_t$. From the Schrödinger equation, we derive [7]

$$\frac{dC}{dt} = i\,\beta(t)\langle[H_d, H_p]\rangle_t = \beta(t)A(t), \tag{2}$$

where $A(t) = i\langle[H_d, H_p]\rangle_t$. By choosing $\beta(t) = -A(t)$, we get $\frac{dC}{dt} = -A(t)^2 \leqslant 0$, which implies the energy expectation decreases monotonically. The evolution operator is

$$U(T) = \mathcal{T}\exp\left[-i\int_0^T (H_p + \beta(t)H_d)dt\right], \tag{3}$$

which, in practice, is implemented via a discrete Trotter expansion as

$$U(t) \approx \prod_{k=0}^{T/\Delta t} e^{-iH_p\Delta t}e^{-i\beta_k H_d\Delta t}, \tag{4}$$

where T denotes the total evolution time, Δt is the discrete Trotter time step, and $\beta_k = -A_{k-1}$, and

$$|\psi_k\rangle = e^{-iH_p\Delta t}e^{-i\beta_{k-1}H_d\Delta t}|\psi_{k-1}\rangle. \tag{5}$$

In a qubit representation, both H_p and H_d can be decomposed into sums of Pauli strings, i.e., $H_p = \sum_\mu c_\mu P_\mu; H_d = \sum_\nu d_\nu Q_\nu$, where P_μ and Q_ν denote tensor products of Pauli operators. Consequently, the commutator $[H_d, H_p]$ can also be written as

$$[H_d, H_p] = \sum_\alpha g_\alpha R_\alpha, \tag{6}$$

allowing β_k to be estimated on quantum hardware through repeated measurements of the corresponding Pauli observables. In practice, commuting Pauli strings may be grouped into common measurement bases to reduce measurement overhead. The total shot count required to estimate β_k with precision ϵ scales as $N_{\text{shots}} \lesssim (\sum_\alpha |g_\alpha|)^2/\epsilon^2$, which grows polynomially with system size for sparse Hamiltonians such as the FH model.

FALQON provides a recursive, measurement-driven update rule that avoids classical parameter optimization like VQE or QAOA [6], with only H_d and Δt as design inputs. In the ideal continuous-time limit, La Salle's invariance principle [22] implies that the dynamics may enter an invariant set in which $\langle[H_d, H_p]\rangle_t = 0$, so that $\beta(t) = 0$ and the energy stops decreasing [10]. This typically occurs once the evolution has reached the ground-state manifold, where the feedback signal naturally vanishes [7].

However, in some cases, the system approaches this regime only asymptotically, i.e., $A(t)$ remains close to zero and may fluctuate around zero at late times as the dynamics approach the invariant set. Consequently, $\beta(t)$ becomes weak and repeatedly changes sign, leading to damped oscillatory dynamics with little additional energy reduction [10]. These residual controls are insufficient to produce net energy descent, causing the optimized energy to level off above ground energy. This behavior often arises in half-filled and strong correlation FH lattices, where particle-hole symmetry generates degenerate low-lying spectra with a strongly suppressed commutator response [10].

III. IMAGINARY-TIME EVOLUTION ENHANCEMENT

A. *i*FALQON protocol

To address the above issue, we incorporate an ITE kick-off scheme. The ITE introduces an effective dissipative dynamics that naturally suppresses excited-state amplitudes and enhances overlap with the ground state [15–21]. The imaginary-time Schrödinger equation, $\partial_\tau|\psi(\tau)\rangle = -H_p|\psi(\tau)\rangle$, is analogous to a diffusion equation, where solution gives

$$|\psi(\tau)\rangle = e^{-H_p\tau}|\psi(0)\rangle = \sum_n c_n e^{-E_n\tau}|n\rangle, \tag{7}$$

where we used $H_p = \sum_n E_n|n\rangle\langle n|$ and $|\psi(0)\rangle = \sum_n c_n|n\rangle$. Here, the higher-energy components decay exponentially faster than the ground state. Taking the limit $\tau \to \infty$ gives $|\psi(\tau)\rangle \to c_0 e^{-E_0\tau}|0\rangle$, which converges to its ground state. Applying the Taylor expansion yields

$$|\Phi_{\Delta\tau}(\psi)\rangle \equiv |\psi(\tau+\Delta\tau)\rangle \approx \frac{(I - H_p\Delta\tau)|\psi(\tau)\rangle}{\|(I - H_p\Delta\tau)|\psi(\tau)\rangle\|}. \tag{8}$$

In our *i*FALQON protocol, we insert Eq. (8) periodically between FALQON steps, yielding

$$|\psi_k\rangle = \mathcal{N}\big[(I - H_p\Delta\tau)e^{-iH_p\Delta t}e^{-i\beta_{k-1}H_d\Delta t}|\psi_{k-1}\rangle\big], \tag{9}$$

where $\mathcal{N}$ is the normalization. The term $(I - \Delta\tau H_p)$ redistributes the population toward lower-energy sectors, reactivating the feedback term $\beta(t)$ and guiding the evolution back to the true ground state. This hybrid real-imaginary dynamics unites Lyapunov stability [8,9] with dissipative convergence toward the energy minimum.

The imaginary-time update $(I - \Delta\tau H_p)$ is nonunitary and therefore cannot be directly implemented as a deterministic quantum gate. In this work, we employ this update only at the state-vector-simulation level rather than a full hardware-compatible implementation, to investigate its algorithmic effect on the FALQON dynamics.

For practical quantum-hardware implementations, a hardware-compatible realization could be achieved using variational quantum imaginary-time evolution (VarQITE),

where the parameters of a trial state $|\psi(\boldsymbol{\theta})\rangle$ are updated according to McLachlan's variational principle [15]. Such implementations generally require additional measurements to estimate the quantum geometric tensor $\mathcal{F}_{ij} = \mathrm{Re}\langle\partial_i\psi|\partial_j\psi\rangle$ and the energy gradient vector $\mathcal{E}_i = -\mathrm{Re}\langle\partial_i\psi|\hat{H}_p|\psi\rangle$, whose costs scale as $\mathcal{O}(N_{\mathrm{params}}^2)$ and $\mathcal{O}(N_{\mathrm{params}} \times N_{\mathrm{Pauli}})$ per update, respectively.

B. Energy-decrease mechanism of the ITE step

In this subsection, we analyze how ITE suppresses excited-state components and lowers the energy during the *i*FALQON dynamics. Let H_p be a bounded, positive semidefinite Hamiltonian with spectral norm $\|H_p\| = \sup_{|\psi|=1}\langle\psi|H_p|\psi\rangle \leqslant h$. The hybrid algorithm alternates infinitesimal imaginary-time updates $|\Phi_{\Delta\tau}(\psi)\rangle$ with the feedback control defined by $\beta(t) = -i\langle[H_d, H_p]\rangle_t$. Then, at every ITE update, the normalized cost function gives

$$C(\Phi_{\Delta\tau}(\psi)) = \frac{\langle(I-\Delta\tau H_p)H_p(I-\Delta\tau H_p)\rangle_\psi}{\langle(I-\Delta\tau H_p)^2\rangle_\psi}, \tag{10}$$

which obeys the bound

$$C(\Phi_{\Delta\tau}(\psi)) \leqslant E - \frac{2\Delta\tau\left(1-\frac{1}{2}h\Delta\tau\right)}{(1-h\Delta\tau)^2}\mathcal{V}, \tag{11}$$

for $0 < \Delta\tau \neq \frac{1}{h} < \frac{2}{h}$, where $E = \langle H_p\rangle_\psi$ and the variance $\mathcal{V} = \langle(H_p - E)^2\rangle_\psi$. The upper bound implies $C(\Phi_{\Delta\tau}(\psi)) < C(\psi)$ whenever $\mathcal{V} > 0$. Thus, the cost function $\{C(\Phi_{\Delta\tau}(\psi_k))\}$ decreases until $\mathcal{V} = 0$.

To derive the bound in Eq. (11), let $E = \langle H_p\rangle_\psi$ the original cost function, $\mathcal{V} = \langle(H_p - E)^2\rangle_\psi$ its variance, and recast $C(\Phi_{\Delta\tau}(\psi)) = \frac{T}{D}$; we have

$$T = E - 2\Delta\tau\langle H_p^2\rangle_\psi + \Delta\tau^2\langle H_p^3\rangle_\psi, \tag{12}$$

$$D = 1 - 2\Delta\tau E + \Delta\tau^2\langle H_p^2\rangle_\psi. \tag{13}$$

Given $H_p \leqslant E_{\max} I$, we have

$$\langle H_p^3\rangle_\psi \leqslant h\langle H_p^2\rangle_\psi, \quad \langle H_p^2\rangle_\psi \geqslant E^2. \tag{14}$$

Hence,

$$\begin{aligned} T &\leqslant E - (2\Delta\tau - \Delta\tau^2 h)\langle H_p^2\rangle_\psi \\ &= E - (2\Delta\tau - \Delta\tau^2 h)(E^2 + \mathcal{V}). \end{aligned} \tag{15}$$

For the denominator, using $\langle H_p^2\rangle_\psi \geqslant E^2$ gives

$$D \geqslant 1 - 2\Delta\tau E + \Delta\tau^2 E^2 = (1-\Delta\tau E)^2 \geqslant (1-\Delta\tau h)^2; \tag{16}$$

thus, for $\Delta\tau \neq \frac{1}{h}$, we have $\frac{1}{D} \leqslant \frac{1}{(1-\Delta\tau h)^2}$. Combining, we get

$$C(\Phi_{\Delta\tau}(\psi)) \leqslant \frac{E - (2\Delta\tau - \Delta\tau^2 h)\mathcal{V} - (2\Delta\tau - \Delta\tau^2 h)E^2}{(1-\Delta\tau h)^2}. \tag{17}$$

For any $0 < \Delta\tau \neq \frac{1}{h} < \frac{2}{h}$, the coefficient $(2\Delta\tau - \Delta\tau^2 h) > 0$. Therefore, $-(2\Delta\tau - \Delta\tau^2 h)E^2 \leqslant 0$, which can be dropped in the numerator, yields the clean, conservative bound

$$C(\Phi_{\Delta\tau}(\psi)) \leqslant \frac{E}{(1-\Delta\tau h)^2} - \frac{2\Delta\tau - \Delta\tau^2 h}{(1-\Delta\tau h)^2}\mathcal{V}. \tag{18}$$

In particular, for sufficiently small $\Delta\tau$, we obtain the first-order decrease

$$C(\Phi_{\Delta\tau}(\psi)) \leqslant E - 2\Delta\tau\mathcal{V} + \mathcal{O}(\Delta\tau^2) \tag{19}$$

and the rigorous decrease

$$C(\Phi_{\Delta\tau}(\psi)) \leqslant E - \frac{2\Delta\tau\left(1-\frac{1}{2}\Delta\tau h\right)}{(1-\Delta\tau h)^2}\mathcal{V}, \tag{20}$$

for all $0 < \Delta\tau \neq \frac{1}{h} < \frac{2}{h}$ and $\mathcal{V} \geqslant 0$.

The above analysis indicates that the imaginary-time step locally suppresses excited-state components and decreases the energy whenever the state has nonzero energy variance. Within the *i*FALQON dynamics, these periodic nonunitary updates help prevent stagnation near degenerate manifolds where the feedback signal becomes weak, thereby improving the overall convergence behavior observed in the numerical simulations.

C. Spectral origin of the ITE reactivation mechanism

The previous subsection showed that an ITE step reduces the cost function for any state with nonzero energy variance. We now examine the spectral mechanism by which ITE restores the FALQON feedback signal $A(t)$ and lowers the cost.

Let $\rho(t)=|\psi(t)\rangle\langle\psi(t)|$, such that $A(t)=i\mathrm{Tr}([H_p, \rho(t)]H_d)$. Using $[H_p, \rho(t)]_{nm} = (E_n - E_m)\rho_{nm}(t)$, we obtain

$$A(t) = -2\sum_{n<m}(E_n - E_m)\,\mathrm{Im}[\rho_{nm}(t)(H_d)_{mn}]. \tag{21}$$

For degenerate eigenstates, $E_n = E_m$, so their contribution to $A(t)$ vanishes. Thus, if the state is confined to a degenerate manifold, $A(t) = 0$ and the FALQON feedback stops.

To describe the contributions between different energy manifolds, we group eigenstates with the same energy into $M_j = \{n : E_n = E_j\}$, with projector Π_j, and define the intermanifold coherence

$$g_{jk}(t) = \mathrm{Tr}\left[\Pi_j\rho(t)\Pi_k H_d\right]. \tag{22}$$

The feedback signal then becomes

$$A(t) = -2\sum_{j<k}(E_j - E_k)\,\mathrm{Im}\,g_{jk}(t). \tag{23}$$

To illustrate the ITE reactivation mechanism, we consider a state concentrated near a degenerate excited manifold M_d, with residual intermanifold coherence $g_{cd}(t)$ connecting M_d to a lower-energy manifold M_c ($E_c < E_d$). Since $K = I - \Delta\tau H_p$ acts uniformly within each energy manifold,

$$K\Pi_j = k_j\Pi_j, \quad k_j = 1 - \Delta\tau E_j. \tag{24}$$

The normalized ITE update $\rho \to K\rho K/D$ then gives

$$g'_{cd} = \frac{k_c k_d}{D}g_{cd}. \tag{25}$$

Near M_d, $D \simeq k_d^2$, and hence

$$g'_{cd} \simeq \frac{k_c}{k_d}g_{cd} = \frac{1-\Delta\tau E_c}{1-\Delta\tau E_d}g_{cd}. \tag{26}$$

For $E_c < E_d$ and $1 - \Delta\tau E_d > 0$, the prefactor is larger than 1, so ITE amplifies $|\mathrm{Im}\,g_{cd}|$. Through Eq. (23), this enhancement

restores the feedback signal and resumes the FALQON energy descent. Equation (26) also shows that the reweighting becomes stronger as $\Delta\tau$ increases within the small-step regime, $\Delta\tau E_d < 1$.

We emphasize that this mechanism differs from stand-alone QITE [15,16], which does not rely on the feedback signal $A(t)$. In *i*FALQON, ITE instead reweights the spectral components that contribute to the FALQON feedback. A direct comparison with stand-alone QITE is presented in the next section.

IV. DEMONSTRATION ON FERMI-HUBBARD MODEL

A. Model

The Fermi-Hubbard model describes interacting fermions on a lattice and captures the competition between kinetic hopping and on-site repulsion. It provides a minimal framework for phenomena such as the Mott transition, antiferromagnetism, and unconventional superconductivity. Its Hamiltonian is

$$H_{\mathrm{FH}} = -J \sum_{\langle i,j\rangle,\sigma} \left(c_{i\sigma}^{\dagger} c_{j\sigma} + c_{j\sigma}^{\dagger} c_{i\sigma}\right) + U \sum_{i} n_{i\uparrow} n_{i\downarrow}, \qquad (27)$$

where J denotes the hopping amplitude between nearest-neighbor sites $\langle i, j\rangle$ and U represents the on-site Coulomb repulsion between fermions of opposite spin. The fermionic creation and annihilation operators $c_{i\sigma}^{\dagger}$ and $c_{i\sigma}$ obey the canonical anticommutation relations $\{c_{i\sigma}, c_{j\sigma'}^{\dagger}\} = \delta_{ij}\delta_{\sigma\sigma'}$, and the local number operator is $n_{i\sigma} = c_{i\sigma}^{\dagger} c_{i\sigma}$.

For a lattice with L sites and particle numbers $N_{\uparrow}$ and $N_{\downarrow}$, the filling is $\nu = N/L$ with $N = N_{\uparrow} + N_{\downarrow}$. Half filling ($\nu = 1$) corresponds to one particle per site on average and typically exhibits strong correlations and insulating behavior at large U/J. In this regime, particle-hole symmetry leads to degenerate low-lying spectra. Away from half filling ($\nu \neq 1$), the system is doped, particle-hole symmetry is broken, and mobile carriers appear, often restoring metallic behavior. In simulations, configurations are specified by the spin populations, e.g., (1, 2) for a three-particle doped case or (2, 2) for the half-filled four-site lattice.

This model captures the essential interplay between kinetic hopping and on-site interaction, making it a prototypical system for studying strongly correlated electrons [23,24], Mott insulators [25–28], and magnetism [29,30]. Despite its simplicity, the model exhibits a rich variety of complex quantum materials. Beyond basic magnetic ordering like ferromagnetism and various forms of antiferromagnetism, it is known to host exotic phases including charge-density waves [31,32], electronic liquid-crystal states with broken rotational symmetry [33–35], and spin-liquid phases in frustrated regimes [36,37]. It also provides a central microscopic framework for unconventional superconductivity [38].

To numerically simulate this system on quantum computers, H_{FH} needs to be formulated in Pauli strings. For an N-site lattice, we use Jordan-Wigner (JW) mapping to encode the $2N$ spin orbitals to $2N$ qubits [39]. This transformation maps local fermionic operators to nonlocal Pauli strings involving chains of Z operators to preserve the anticommutation relations. Consequently, the hopping terms in the Hamiltonian are transformed into multiqubit strings, while on-site interactions are mapped to local diagonal terms. The explicit derivation and the full form of the mapped Hamiltonian are provided in the Appendix.

After mapping the fermions to qubits, we simulate ground-state preparation directly on quantum registers. We focus on the strongly correlated regime $U/J = 5.0$, which lies deep in the Mott insulating phase [25–28]. In this regime, charge fluctuations are suppressed and spin correlations dominate, generating strong entanglement that is beyond the reach of mean-field methods, tensor-network truncations, and Monte Carlo techniques [40–42].

Our benchmarking area includes linear one-dimensional (1D) lattices ([1×3], [1×4], and [1×5]) and square two-dimensional (2D) lattices ([2×2], [2×3], and [3×3]). Hereafter, $[i\times j]$ labels the lattice size, and (k, l) indicates the number of spin-up and spin-down fermions, $N_{\uparrow}$ and $N_{\downarrow}$, respectively. For example, the largest [3×3](4, 5) lattice corresponds to 9 lattice sites and 18 spin orbitals, requiring 18 qubits after the JW transformation. All simulations were performed using the Qiskit state vector simulator, providing a noiseless benchmark of algorithmic performance without decoherence, sampling noise, or thermal fluctuations. Therefore, the results here interpret as proof-of-concept demonstrations of the *i*FALQON framework. We set $H_p = H_{\mathrm{FH}}$ and use the hopping term $H_d = -J \sum_{\langle i,j\rangle,\sigma} (c_{i\sigma}^{\dagger} c_{j\sigma} + \mathrm{H.c.})$, which conserves particle number while not commuting with H_p, thereby enabling effective state transitions.

B. FALQON without ITE

Figure 1 shows the dynamical behavior of FALQON without ITE, evaluated various FH lattice geometries and fillings. Figure 1(a) plots the time evolution of the energy difference $\Delta E(t) = E(t) - E_0$, where E_0 is the exact ground-state energy obtained from exact diagonalization of H_{FH}, and $E(t) = \langle H_{\mathrm{FH}}\rangle_t$.

For small and moderately asymmetric lattices such as [1×3], [1×4], [1×5], and [2×3], $\Delta E(t)$ decays exponentially over several orders of magnitude, reaching values below 10^{-2} at $t = 10^3$. This monotonic decay confirms that FALQON efficiently drives the system toward its true ground state through the self-consistent feedback law $\beta(t) = -A(t)$.

For the [2×2] lattice, the behavior depends strongly on the filling configuration. In the doped configuration [2×2] (1, 2), the particle-hole symmetry breaks, and thus the convergence remains exponential, similar to asymmetric lattices. In contrast, the half-filled case [2×2] (2, 2) shows a plateau of $\Delta E(t)$ above 10^0. This behavior indicates that the evolution has entered an invariant subspace in which the expectation value of the commutator $A(t) = i\langle[H_d, H_p]\rangle_t$ averages to zero [see the inset in Fig. 1(b)].

For the [3×3] lattice, both doped and half-filled configurations show a similar convergence plateau. After an initial transient decay, $\Delta E(t)$ flattens into a broad plateau as the feedback amplitude diminishes, and the system remains stuck above the ground-state manifold.

Figure 1(b) displays the time evolution of the feedback field $\beta(t)$. The signal initially rises in response to large values of the commutator $A(t)$, and subsequently decreases as

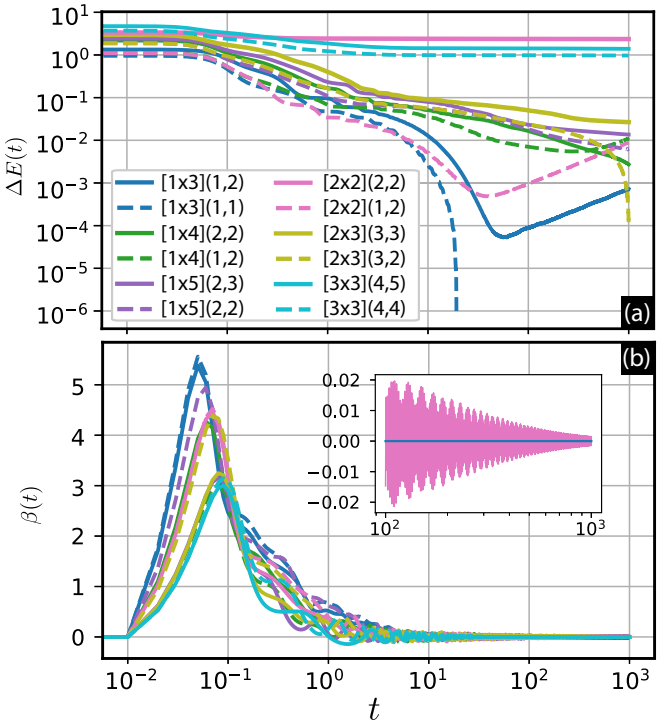


FIG. 1. Dynamics of the FALQON without ITE. (a) Time evolution of the energy difference $\Delta E(t) = E(t) - E_0$ for various FH lattices and fillings. Doped systems ([1×3], [1×4], and [2×3]) exhibit smooth exponential convergence toward the exact ground energy, while half-filled configurations ([2 × 2], [3 × 3]) stagnate at finite energy errors. (b) Corresponding feedback amplitude $\beta(t)$ as defined by the Lyapunov control law $\beta(t) = -A(t)$. The early peak in $\beta(t)$ accelerates energy descent, but in half-filled lattices the feedback collapses to zero prematurely, halting further optimization. The inset shows long-time oscillations of $\beta(t)$ for the [2×2] and [3×3] cases, demonstrating symmetric fluctuations around zero and confirming feedback quenching due to degeneracy. Together, these results reveal that pure FALQON effectively prepares ground states only for nondegenerate systems, motivating the introduction of an imaginary-time enhancement. In the legend, $[i\times j]$ stands for the lattice site and (k, l) stands for $(N_\uparrow, N_\downarrow)$.

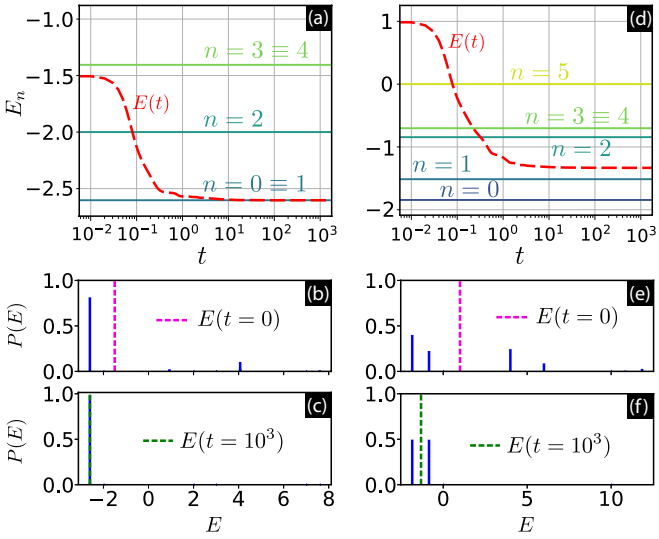


FIG. 2. Energy spectra and population dynamics for the doped and half-filled [2×2] FH systems under FALQON without ITE. (a), (d) Mean energy $E(t)$ (dashed red) overlaid on the energy spectra E_n of H_{FH}. In the doped case [panel (a)], $E(t)$ descends toward the ground state without crossing any degenerate levels. In the half-filled case [panel (d)], $E(t)$ crosses a manifold of degenerate excited states, suppressing the feedback response and halting further relaxation. (b), (c) Probability distributions $P(E)$ at $t = 0$ and $t = 10^3$ for the doped system, showing collapse into the ground state. (e), (f) Corresponding distributions for the half-filled system, where significant weight remains in low-lying excited states due to trapping within a subspace.

the system approaches a stationary regime. In trajectories that successfully converge to the ground-state energy, $\beta(t)$ smoothly decays to zero. In contrast, in nonconvergent cases where the dynamics become trapped in a local minimum, $\beta(t)$ settles into small oscillations around zero. The inset compares $\beta(t)$ for the [2×2](2, 2) and [1×3](1, 2) configurations over $t \in [10^2, 10^3]$, showing that the former exhibits rapidly damped oscillations about zero, whereas the latter displays a monotonic decay toward zero.

To further elucidate the behavior in Fig. 1, we examine the energy spectrum $\{E_n\}$ of H_{FH}, i.e., $H_{\mathrm{FH}} = \sum_n E_n |n\rangle\langle n|$, and the populations $P(E) = |\langle n|\psi(t)\rangle|^2$ for the [2×2] doped and half-filled systems. Figures 2(a)–2(c) correspond to the doped configuration (1, 2), while Figs. 2(d)–2(f) show the half-filled case (2, 2).

In the doped case shown in Fig. 2(a), the low-lying spectrum exhibits several twofold degeneracies, including $E_0 = E_1$ and $E_3 = E_4$. Remarkably, the trajectory of the mean energy $E(t) = \langle H_{\mathrm{FH}}\rangle_t$ decreases monotonically toward the ground-state manifold without crossing any of these degenerate levels except $E_0 = E_1 =$ ground energy. The absence of degeneracy crossings ensures that $A(t)$ remains finite throughout the evolution, enabling the feedback field to continue directing population toward lower energies. As shown in Figs. 2(b) and 2(c), the initially broad energy distribution $P(E)$ rapidly collapses into a sharply peaked ground-state population by $t = 10^3$. This behavior aligns with the exponential decay of $\Delta E(t)$ in Fig. 1(a) and demonstrates that FALQON achieves reliable ground-state preparation in the doped configuration.

In contrast, the half-filled system shown in Fig. 2(d) exhibits a qualitatively different mechanism. Here, the trajectory $E(t)$ encounters a manifold of degenerate excited states, such as the pair $E_3 = E_4$. Once $E(t)$ enters this degenerate sector, $A(t)$ becomes strongly suppressed, and the resulting feedback field $\beta(t)$ decays toward zero with only weak residual oscillations. These small controls are insufficient to induce transitions out of the degenerate manifold, causing the energy evolution to trap above the true ground energy. The probability distributions in Figs. 2(e) and 2(f) further confirm this behavior, where even at long times, the population remains distributed over several low-lying excited states rather than concentrating at E_0. Thus, in the half-filled configuration, the trajectory becomes trapped in a local subspace after crossing a degenerate manifold, preventing full relaxation to the ground state.

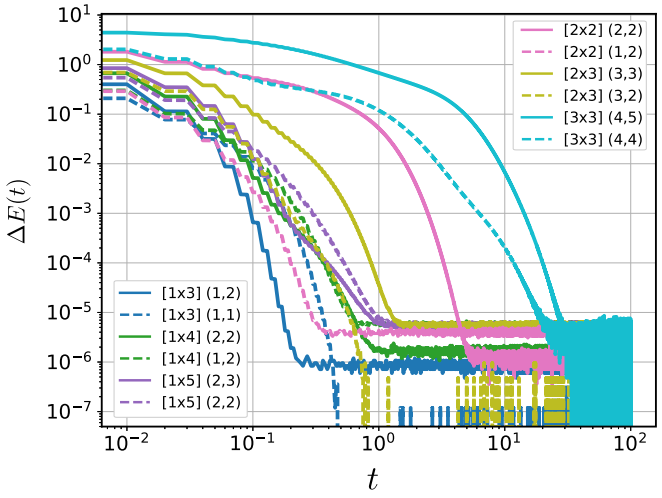


FIG. 3. Energy convergence of the *i*FALQON. Time evolution of the energy difference $\Delta E(t) = E(t) - E_0$ for various FH lattices. An imaginary-time step of $\Delta\tau = 0.05$ is inserted after every two feedback layers. All configurations now converge monotonically toward the exact ground energy, reaching relative errors below 10^{-5}. The exponential decay across more than six decades confirms that *i*FALQON restores stable ground-state preparation.

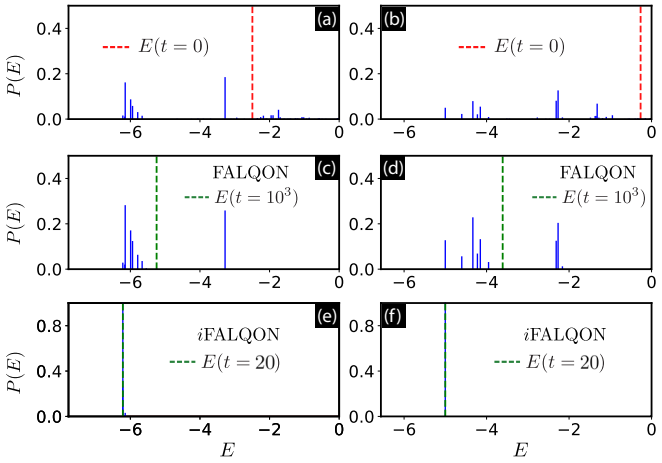


FIG. 4. Energy distributions for the [3×3] FH lattice. (a), (b) Initial energy populations for doped and half-filled configurations, showing dominant support at high excited levels above the ground state (red dashed line). (c), (d) Final distributions under pure FALQON remain spread over excited states, indicating failure to reach the ground state. (e), (f) *i*FALQON collapses the distributions onto the ground state, demonstrating successful convergence.

C. *i*FALQON

Figure 3 shows the energy difference $\Delta E(t)=E(t)-E_0$ for all tested lattices under the *i*FALQON protocol. An imaginary-time step of $\Delta\tau = 0.05$ is applied after every two feedback layers. Unlike the behavior in Fig. 1, all trajectories now exhibit a clean monotonic exponential decay. Systems from one-dimensional chains $[1\times3] - [1\times5]$ to two-dimensional lattices $[2\times2]$, $[2\times3]$, $[3\times3]$ converge to the exact ground-state energy with final errors below 10^{-5}. Crucially, the $[2\times2](2, 2)$ and $[3\times3](k, l)$ cases, both of which stalled under pure FALQON, now follow the same smooth descent as the other configurations. The ITE step accelerates convergence by continuously shifting amplitude toward lower energies, shortening the relaxation time. This result shows that hybrid real-imaginary-time feedback improves ground-state convergence, making *i*FALQON as a robust framework for strongly correlated quantum systems.

D. [3×3] lattice FH model

This is the most strongly correlated system considered in this work, and its convergence behavior under pure FALQON remains poor for both doped and half-filled configurations, as shown in the main text. To clarify the origin of this failure, Fig. 4 displays the probability distributions over the energy eigenbasis at the beginning and end of the FALQON evolution.

The upper panels show the initial energy distributions for the doped [panel (a)] and half-filled [panel (b)] configurations. In both cases, the initial state carries substantial weight across high-energy excited levels, with dominant support well above the ground energy (red dashed line). Such broad high-energy populations require the FALQON dynamics to transfer probability across many levels, which becomes increasingly difficult on larger correlated lattices.

The middle panels (c) and (d) show the final energy distributions after a long FALQON evolution. In contrast to smaller lattices discussed in the main text, the [3×3] system fails to concentrate probability near the ground state. Although some redistribution occurs, substantial weight remains on excited levels and the dominant peaks lie far above the ground energy (green dashed line). This persistent high-energy support matches the plateau in $\Delta E(t)$ and indicates that the feedback updates cannot drive transitions across the densely packed low-lying spectrum of the [3×3] lattice.

The bottom panels (e) and (f) display the final distributions under *i*FALQON. In this case, both configurations successfully converge to the ground state, and the transition occurs noticeably faster than in the pure FALQON protocol.

These distributions show that, on the [3×3] lattice, pure FALQON is unable to drive the wave function into the low-energy sector. However, introducing periodic imaginary-time steps (*i*FALQON) suppresses high-energy amplitudes and enables population flow toward the ground state.

E. Comparison with stand-alone imaginary-time evolution

We next compare *i*FALQON with stand-alone QITE [15,16]. Both methods start from the same initial state and use the same first-order imaginary-time update. We define the ITE insertion period f as the number of FALQON steps between two time ITE updates, with $f = 1$ corresponding to an ITE update after every FALQON step.

Figure 5(a) shows the energy error $\Delta E(t) = E(t) - E_0$ for the doped $[2 \times 2](1, 2)$ and half-filled $[2 \times 2](2, 2)$ configurations at $\Delta\tau = 0.05$. In stand-alone QITE, each evolution step is an ITE update, while for *i*FALQON we consider insertion periods $f = 1, 3$, and 5. Increasing f slows the convergence because ITE updates are applied less frequently.

We next examine how the ITE insertion period affects the number of ITE updates required to reach a given accuracy. To

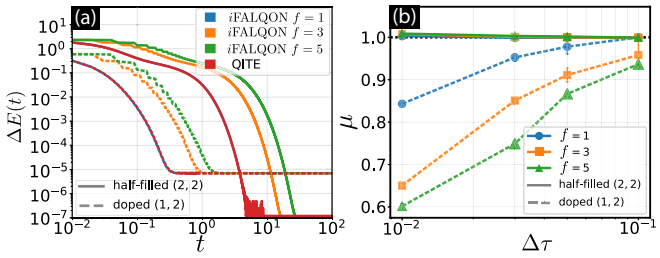


FIG. 5. Comparison of *i*FALQON and stand-alone QITE on the [2 × 2] FH lattice. (a) Energy error $\Delta E(t) = E(t) - E_0$ for the half-filled (2, 2) (solid lines) and doped (1, 2) (dashed lines) configurations at $\Delta\tau = 0.05$. *i*FALQON is shown for ITE insertion periods $f = 1, 3$, and 5, while stand-alone QITE applies an ITE update at every step. (b) Ratio $\mu = N_{\text{ITE}}^{i\text{FALQON}}/N_{\text{ITE}}^{\text{QITE}}$ of the number of ITE updates required to reach $\Delta E < 10^{-5}$ as a function of $\Delta\tau$.

quantify this effect, Fig. 5(b) shows

$$\mu = \frac{N_{\text{ITE}}^{i\text{FALQON}}}{N_{\text{ITE}}^{\text{QITE}}}, \tag{28}$$

where N_{ITE} is the number of ITE updates required to reach $\Delta E < 10^{-5}$. Thus, $\mu < 1$ means that *i*FALQON requires fewer ITE updates than stand-alone QITE.

For the doped configuration, μ decreases with increasing f, reaching approximately 0.60 at $f = 5$ and $\Delta\tau = 0.01$. In contrast, μ remains close to one at half filling over the tested range of f and $\Delta\tau$. Thus, the FALQON evolution reduces the required number of ITE updates when the feedback remains active, as shown in the doped case. However, there is no such reduction when the feedback is suppressed at half filling.

A reduction in the number of ITE updates does not imply a lower total computational cost, since *i*FALQON also involves FALQON evolution. We estimate the costs as

$$\begin{aligned} \mathcal{C}_{i\text{FALQON}} &= N_{\text{ITE}}^{i\text{FALQON}}\mathcal{C}_{\text{ITE}} + N_{\text{F}}\mathcal{C}_{\text{F}}, \\ \mathcal{C}_{\text{QITE}} &= N_{\text{ITE}}^{\text{QITE}}\mathcal{C}_{\text{ITE}}, \end{aligned} \tag{29}$$

where $\mathcal{C}_{\text{ITE}}$ and $\mathcal{C}_{\text{F}}$ denote the costs of one ITE and FALQON step, respectively. The equal-cost condition, $\mathcal{C}_{i\text{FALQON}} = \mathcal{C}_{\text{QITE}}$, is

$$N_{\text{F}}\mathcal{C}_{\text{F}} = (1 - \mu)\mathcal{C}_{\text{QITE}}. \tag{30}$$

Thus, the two methods have the same total cost only when the FALQON cost equals the cost saved by fewer ITE updates.

As discussed in Sec. III A, a QITE implementation requires measurements of the quantum geometric tensor $\mathcal{F}_{ij}$ and energy gradient $\mathcal{E}_i$, with the costs scaling as $\mathcal{O}(N_{\text{params}}^2)$ and $\mathcal{O}(N_{\text{params}}N_{\text{Pauli}})$, respectively, per update. In *i*FALQON, the FALQON step instead evaluates the feedback signal $A(t)$, which requires $\mathcal{O}(N_{\text{Pauli}})$, where N_{Pauli} is the number of Pauli terms in $i[H_d, H_p]$. A hardware-level comparison accounts for the circuit and measurement costs of the FALQON steps and depends on the specific ITE implementation, which is beyond our state vector simulations.

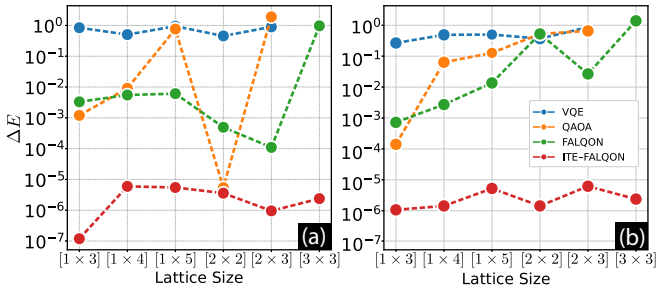


FIG. 6. Benchmarking between QAOA, VQE, FALQON, and *i*FALQON: Energy error $\Delta E = E - E_0$ as a function of lattice size for the FH model. (a) The doped regime and (b) the half-filling case. Results are shown for VQE (EHV ansatz), QAOA, FALQON, and the proposed *i*FALQON protocol.

V. BENCHMARKING

In this section, we compare the performance of the *i*FALQON model with other existing approaches, including QAOA and VQE.

A. FH model

Figure 6 summarizes the benchmarking results for ground-state energy estimation of the FH model across different lattice sizes for various frameworks, including QAOA, VQE, FALQON, and *i*FALQON. Figure 6(a) corresponds to the doped regime, while Fig. 6(b) shows the half-filling case. The energy error is defined as $\Delta E = E - E_0$, where E_0 denotes the exact ground-state energy and E denotes the final energy at the last iteration.

QAOA and VQE are both hybrid quantum-classical algorithms based on unitary variational ansätze optimized through a classical feedback loop. In QAOA, the trial state is constructed by applying $p = 8$ alternating layers of time evolution under the problem Hamiltonian H_c and a noncommuting mixer Hamiltonian H_d. We adopt the same Hamiltonian formulations for H_c and H_d as used in FALQON. The parameters are optimized using the COBYLA optimizer over 5000 iterations.

VQE employs a parametrized quantum circuit to minimize the energy expectation value of the Hamiltonian. We use the efficient Hamiltonian variational (EHV) ansatz to reduce circuit depth arising from the JW transformation. The simulation is executed with $p = 5$ layers, where optimization process consists of 2000 COBYLA steps.

These limitations are clearly reflected in Fig. 6. In both the doped [panel (a)] and half-filled [panel (b)] regimes, QAOA and VQE exhibit relatively large energy errors that vary weakly with lattice size. In particular, QAOA shows pronounced fluctuations, indicating difficulty in maintaining consistent convergence across different lattice geometries. VQE yields more stable results but remains confined to an error floor set by the expressibility of the ansatz and the optimization process.

The original FALQON protocol improves upon variational methods by replacing global optimization with feedback-based unitary evolution. In the doped regime, FALQON achieves moderate error reduction for certain lattice sizes

but displays noticeable performance variability. At half filling, where the ground state exhibits stronger correlations and enhanced symmetry constraints, the purely unitary feedback dynamics become less effective, leading to a degradation in accuracy for larger lattices.

In contrast, the *i*FALQON framework achieves lower energy errors than the compared methods for the tested systems. By incorporating imaginary-time evolution into the feedback protocol, excited-state components are exponentially suppressed, enabling rapid convergence toward the ground state. As shown in Fig. 6, the resulting energy error remains at the level of 10^{-6} to 10^{-7} across all lattice sizes, with only weak dependence on filling fraction or system geometry.

The comparison between Figs. 6(a) and 6(b) further highlights the robustness of *i*FALQON. While variational and unitary methods exhibit increased sensitivity at half filling due to stronger many-body correlations, *i*FALQON maintains uniform performance. This demonstrates that nonunitary, feedback-assisted evolution provides a robustness for ground-state preparation in strongly correlated fermionic systems.

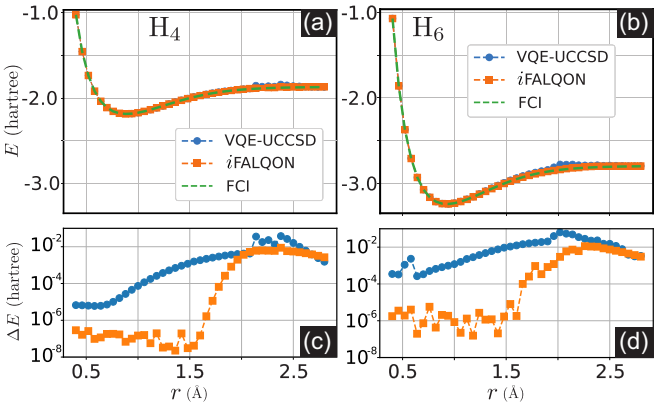


FIG. 7. *i*FALQON accurately reproduces the ground-state potential energy surfaces of hydrogen chains. Ground-state potential energy of the hydrogen chains H_4 [panel (a)] and H_6 [panel (b)] as a function of the interatomic distance r, obtained using *i*FALQON, VQE-UCCSD, and FCI. The corresponding energy errors relative to FCI are shown in panel (c) for H_4 and in panel (d) for H_6.

B. Ground-state potential energy of hydrogen chains

To assess the performance of the *i*FALQON on molecular systems, we benchmark the ground-state potential energy surfaces of hydrogen chains, H_4 and H_6, in the STO-3G basis. The interatomic distance r between nearest-neighbor hydrogen atoms is varied from 0.4 to 2.8 Å, spanning both the weakly correlated equilibrium region and the strongly correlated stretched regime. These systems provide standard yet challenging test beds for evaluating the robustness of ground-state solvers in the presence of electron correlation.

The performance of *i*FALQON is compared against the VQE and the full configuration interaction (FCI) reference. For the VQE simulations, we employ the unitary coupled-cluster ansatz with single and double excitations (UCCSD) [2,43], with parameters optimized using the Adam optimizer at a learning rate of 0.1 for 200 iterations (for H_4) and 1000 iterations (for H_6) at each molecular geometry. For *i*FALQON, the simulations are carried out with a total evolution time $T = 100$, a time step $dt = 0.005$, and an imaginary-time increment $\Delta\tau = 0.15$ applied every two FALQON steps.

As shown in Figs. 7(a) and 7(b), *i*FALQON reproduces the FCI ground-state potential energy curves of the hydrogen chains H_4 and H_6 with high accuracy over the full range of interatomic distances r. The agreement holds both near equilibrium and deep in the stretched regime, where strong electronic correlations become significant. In contrast, the VQE-UCCSD exhibits noticeable deviations from the FCI curve as r increases, particularly for H_6, where the variational optimization becomes increasingly unstable and sensitive to the choice of ansatz and optimizer [43–45].

The corresponding energy deviations relative to FCI, displayed in Figs. 7(c) and 7(d), further demonstrate the robustness of *i*FALQON, which maintains small and smooth errors across all bond lengths for both systems. In contrast, VQE-UCCSD exhibits increasingly large and nonuniform deviations as r increases, most prominently for H_6, indicating reduced stability in the strongly correlated regime.

These results illustrate the advantage of *i*FALQON's feedback-assisted imaginary-time evolution, which mitigates optimization instabilities and avoids the sensitivity to ansatz choice and optimizer settings commonly encountered in variational approaches [43–45]. Compared with stand-alone QITE approaches, *i*FALQON retains the feedback-driven dynamics of FALQON while applying imaginary-time updates only periodically, potentially reducing the number of costly imaginary-time optimization steps while still improving convergence. As system size and correlation strength grow, *i*FALQON maintains stable convergence and reliable energy estimates, highlighting its effectiveness for near-term quantum simulations of strongly correlated molecular systems.

VI. CONCLUSION

We have shown that FALQON converges reliably only when the energy trajectory avoids spectral degeneracies. If the Hamiltonian contains degenerate eigenlevels and the optimal descent path crosses such a manifold, the feedback signal becomes strongly oscillate and the dynamics are trapped within the corresponding degenerate subspace, preventing relaxation to the true ground state. By introducing short imaginary-time steps, the *i*FALQON scheme overcomes this obstruction, gradually reducing excited-state contributions and achieving high-fidelity ground-state preparation across all tested lattices. This hybrid real-imaginary-time framework therefore offers a robust approach to ground-state preparation in strongly correlated quantum systems. The present work focuses on noiseless state vector simulations and small-to-intermediate system sizes, emphasizing the algorithmic behavior of *i*FALQON rather than a detailed hardware-resource analysis. Practical implementations will require balancing the improved convergence provided by the ITE steps against their additional measurement and optimization costs. Extending the framework to noisy quantum hardware, larger lattices, and measurement-limited settings remains an important direction for future work.

ACKNOWLEDGMENTS

This paper was supported by the Tohoku Initiative for Fostering Global Researchers for Interdisciplinary Sciences (TI-FRIS) of MEXT's Strategic Professional Development Program for Young Researchers. L.N.T. was funded by Vietnam National University, Ho Chi Minh City (VNU-HCM) under Grant No. B2026-18-18. T.N.V.L. acknowledges helpful discussions with Vo Minh Phuoc regarding the VQE performance of the H_4 and H_6 molecules, and with Mai Nguyen Phuong Nhi on the FALQON method.

DATA AVAILABILITY

The data that support the findings of this article are openly available [46].

APPENDIX: JORDAN-WIGNER MAPPING

The Jordan-Wigner mapping converts fermionic operators into qubit operators. Each qubit stores whether a fermionic orbital is empty or occupied: $|0\rangle$ = empty, $|1\rangle$ = occupied. To preserve the fermionic anticommutation rule $\{c_i, c_j^\dagger\} = \delta_{ij}$, every operator carries a string of Z gates that counts the parity of all fermions before it. For a system with N qubits, the mapping is

$$c_j = Z^{\otimes(j-1)} \otimes \sigma_j^- \otimes I^{\otimes(N-j)}, \tag{A1}$$

$$c_j^\dagger = Z^{\otimes(j-1)} \otimes \sigma_j^+ \otimes I^{\otimes(N-j)}, \tag{A2}$$

where $\sigma_j^\pm = \frac{1}{2}(X_j \pm iY_j)$.

For the number operator $n_{i\sigma} = c_{i\sigma}^\dagger c_{i\sigma}$, the JW mapping gives $n_{i\sigma} = \frac{I - Z_{i\sigma}}{2}$. Therefore, the on-site interaction term becomes a diagonal qubit operator

$$n_{i\uparrow} n_{i\downarrow} = \tfrac{1}{4}(I - Z_{i\uparrow})(I - Z_{i\downarrow}). \tag{A3}$$

The hopping term $c_i^\dagger c_j + c_j^\dagger c_i$ $(i < j)$ involves the product of operators at different sites. The parity strings Z cancel out on indices $k < i$ and $k > j$, leaving a string of Z operators only on the qubits between i and j:

$$c_i^\dagger c_j + c_j^\dagger c_i = \tfrac{1}{2}(X_i Z_{i+1} \cdots Z_{j-1} X_j + Y_i Z_{i+1} \cdots Z_{j-1} Y_j).$$

This parity string ensures that exchanging two fermions produces the correct minus sign. Combining both parts, the mapped FH Hamiltonian reads

$$H_{\mathrm{FH}} = -\frac{J}{2} \sum_{\langle i,j \rangle} (X_i X_j + Y_i Y_j) Z_{i+1} \cdots Z_{j-1} + \frac{U}{4} \sum_{\langle a,b \rangle} (I - Z_a)(I - Z_b), \tag{A4}$$

where $\langle i, j \rangle$ enumerates qubit indices corresponding to neighboring lattice sites (same spin) and $\langle a, b \rangle$ denotes the qubits encoding spin-up and spin-down orbitals at the same site.

[1] F. Evers and A. D. Mirlin, Anderson transitions, Rev. Mod. Phys. **80**, 1355 (2008).

[2] S. McArdle, S. Endo, A. Aspuru-Guzik, S. C. Benjamin, and X. Yuan, Quantum computational chemistry, Rev. Mod. Phys. **92**, 015003 (2020).

[3] A. Peruzzo, J. McClean, P. Shadbolt, M.-H. Yung, X.-Q. Zhou, P. J. Love, A. Aspuru-Guzik, and J. L. O'Brien, A variational eigenvalue solver on a photonic quantum processor, Nat. Commun. **5**, 4213 (2014).

[4] E. Farhi, J. Goldstone, and S. Gutmann, A quantum approximate optimization algorithm, arXiv:1411.4028.

[5] J. R. McClean, S. Boixo, V. N. Smelyanskiy, R. Babbush, and H. Neven, Barren plateaus in quantum neural network training landscapes, Nat. Commun. **9**, 4812 (2018).

[6] M. Cerezo, A. Arrasmith, R. Babbush, S. C. Benjamin, S. Endo, K. Fujii, J. R. McClean, K. Mitarai, X. Yuan, L. Cincio, and P. J. Coles, Variational quantum algorithms, Nat. Rev. Phys. **3**, 625 (2021).

[7] A. B. Magann, K. M. Rudinger, M. D. Grace, and M. Sarovar, Feedback-based quantum optimization, Phys. Rev. Lett. **129**, 250502 (2022).

[8] D. Dong and I. Petersen, Quantum control theory and applications: A survey, IET Control Theory Appl. **4**, 2651 (2010).

[9] S. C. Hou and X. X. Yi, Quantum Lyapunov control with machine learning, Quantum Inf. Proc. **19**, 8 (2020).

[10] J. B. Larsen, M. D. Grace, A. D. Baczewski, and A. B. Magann, Feedback-based quantum algorithms for ground state preparation, Phys. Rev. Res. **6**, 033336 (2024).

[11] S. X. Li, W. L. Mu, J. B. You, and X. Q. Shao, Simulation of a feedback-based algorithm for quantum optimization for a realistic neutral-atom system with an optimized small-angle controlled-phase gate, Phys. Rev. A **109**, 062603 (2024).

[12] S. Abdul Rahman, Ö. Karabacak, and R. Wisniewski, Feedback-based quantum algorithm for constrained optimization problems, in *Parallel Processing and Applied Mathematics*, edited by R. Wyrzykowski, J. Dongarra, E. Deelman, and K. Karczewski, Lecture Notes in Computer Science Vol. 15580 (Springer, Cham, 2025), pp. 277–289.

[13] H. R. Grimsley, S. E. Economou, E. Barnes, and N. J. Mayhall, An adaptive variational algorithm for exact molecular simulations on a quantum computer, Nat. Commun. **10**, 3007 (2019).

[14] J. Hubbard, Electron correlations in narrow energy bands, Proc. R. Soc. (London), Ser. A **276**, 238 (1963).

[15] S. McArdle, T. Jones, S. Endo, Y. Li, S. C. Benjamin, and X. Yuan, Variational ansatz-based quantum simulation of imaginary time evolution, npj Quantum Inf. **5**, 75 (2019).

[16] M. Motta, C. Sun, A. T. K. Tan, M. J. O'Rourke, E. Ye, A. J. Minnich, F. G. S. L. Brandão, and G. K.-L. Chan, Determining eigenstates and thermal states on a quantum computer using quantum imaginary time evolution, Nat. Phys. **16**, 205 (2020).

[17] N. Gomes, A. Mukherjee, F. Zhang, T. Iadecola, C.-Z. Wang, K.-M. Ho, P. P. Orth, and Y.-X. Yao, Adaptive variational quantum imaginary time evolution approach for ground state preparation, Adv. Quantum Technol. **4**, 2100114 (2021).

[18] S.-N. Sun, M. Motta, R. N. Tazhigulov, A. T. Tan, G. K.-L. Chan, and A. J. Minnich, Quantum computation of finite-temperature static and dynamical properties of spin systems using quantum imaginary time evolution, PRX Quantum **2**, 010317 (2021).

[19] K. Yeter-Aydeniz, R. C. Pooser, and G. Siopsis, Practical quantum computation of chemical and nuclear energy levels using quantum imaginary time evolution and Lanczos algorithms, npj Quantum Inf. **6**, 63 (2020).

[20] H. Nishi, T. Kosugi, and Y.-I. Matsushita, Implementation of quantum imaginary-time evolution method on NISQ devices by introducing nonlocal approximation, npj Quantum Inf. **7**, 85 (2021).

[21] H. Kamakari, S.-N. Sun, M. Motta, and A. J. Minnich, Digital quantum simulation of open quantum systems using quantum imaginary–time evolution, PRX Quantum **3**, 010320 (2022).

[22] J. P. La Salle, *The Stability of Dynamical Systems* (Society for Industrial and Applied Mathematics, Philadelphia, PA, USA, 1976).

[23] Y. A. Izyumov, Hubbard model of strong correlations, Phys. Usp. **38**, 385 (1995).

[24] A. Georges, G. Kotliar, W. Krauth, and M. J. Rozenberg, Dynamical mean-field theory of strongly correlated fermion systems and the limit of infinite dimensions, Rev. Mod. Phys. **68**, 13 (1996).

[25] P. A. Lee, N. Nagaosa, and X.-G. Wen, Doping a Mott insulator: Physics of high-temperature superconductivity, Rev. Mod. Phys. **78**, 17 (2006).

[26] S. Rachel and K. Le Hur, Topological insulators and Mott physics from the Hubbard interaction, Phys. Rev. B **82**, 075106 (2010).

[27] Y.-F. Song, Y. Deng, and Y.-Y. He, Extended metal-insulator crossover with strong antiferromagnetic spin correlation in half-filled 3D Hubbard model, Phys. Rev. Lett. **134**, 016503 (2025).

[28] C. Feng, E. Ibarra-García-Padilla, K. R. A. Hazzard, R. Scalettar, S. Zhang, and E. Vitali, Metal-insulator transition and quantum magnetism in the SU(3) Fermi-Hubbard model, Phys. Rev. Res. **5**, 043267 (2023).

[29] M. Gall, N. Wurz, J. Samland, C. F. Chan, and M. Köhl, Competing magnetic orders in a bilayer Hubbard model with ultracold atoms, Nature (London) **589**, 40 (2021).

[30] Q. Chen, S. A. Chen, and Z. Zhu, Geometric frustration assisted kinetic ferromagnetism in doped Mott insulators, Commun. Phys. **8**, 398 (2025).

[31] F. Ferrari, F. Becca, and R. Valentí, Charge density waves in kagome-lattice extended Hubbard models at the Van Hove filling, Phys. Rev. B **106**, L081107 (2022).

[32] C. van Efferen, J. Berges, J. Hall, E. van Loon, S. Kraus, A. Schobert, T. Wekking, F. Huttmann, E. Plaar, N. Rothenbach, K. Ollefs, L. M. Arruda, N. Brookes, G. Schönhoff, K. Kummer, H. Wende, T. Wehling, and T. Michely, A full gap above the Fermi level: The charge density wave of monolayer VS_2, Nat. Commun. **12**, 6837 (2021).

[33] E. Fradkin, S. A. Kivelson, M. J. Lawler, J. P. Eisenstein, and A. P. Mackenzie, Nematic Fermi fluids in condensed matter physics, Annu. Rev. Condens. Matter Phys. **1**, 153 (2010).

[34] V. Oganesyan, S. A. Kivelson, and E. Fradkin, Quantum theory of a nematic Fermi fluid, Phys. Rev. B **64**, 195109 (2001).

[35] G. P. Alexander, B. G.-G. Chen, E. A. Matsumoto, and R. D. Kamien, *Colloquium*: Disclination loops, point defects, and all that in nematic liquid crystals, Rev. Mod. Phys. **84**, 497 (2012).

[36] L. Savary and L. Balents, Quantum spin liquids: A review, Rep. Prog. Phys. **80**, 016502 (2017).

[37] Y. Zhou, K. Kanoda, and T.-K. Ng, Quantum spin liquid states, Rev. Mod. Phys. **89**, 025003 (2017).

[38] D. P. Arovas, E. Berg, S. A. Kivelson, and S. Raghu, The Hubbard model, Annu. Rev. Condens. Matter Phys. **13**, 239 (2022).

[39] P. Jordan and E. Wigner, Über das paulische äquivalenzverbot, Z. Phys. **47**, 631 (1928).

[40] U. Schollwöck, The density-matrix renormalization group in the age of matrix product states, Ann. Phys. **326**, 96 (2011).

[41] R. Orús, Tensor networks for complex quantum systems, Nat. Rev. Phys. **1**, 538 (2019).

[42] M. Troyer and U.-J. Wiese, Computational complexity and fundamental limitations to fermionic quantum Monte Carlo simulations, Phys. Rev. Lett. **94**, 170201 (2005).

[43] B. Bauer, S. Bravyi, M. Motta, and G. K.-L. Chan, Quantum algorithms for quantum chemistry and quantum materials science, Chem. Rev. **120**, 12685 (2020).

[44] H. G. A. Burton, D. Marti-Dafcik, D. P. Tew, and D. J. Wales, Exact electronic states with shallow quantum circuits from global optimisation, npj Quantum Inf. **9**, 75 (2023).

[45] Y. Fan, C. Cao, X. Xu, Z. Li, D. Lv, and M.-H. Yung, Circuit-depth reduction of unitary-coupled-cluster ansatz by energy sorting, J. Phys. Chem. Lett. **14**, 9596 (2023).

[46] T. N. V. Long, L. N. Tran, and L. B. Ho, Supporting data for "Imaginary-time-enhanced feedback-based quantum algorithms for universal ground-state preparation", GitHub, 2025, https://github.com/echkon/ite_falqon.